Hindawi
International Journal of Aerospace Engineering
Volume 2019, Article ID 2593602, 12 pages
https://doi.org/10.1155/2019/2593602

Research Article

A Model for Igniter Mass Flow Rate History Evaluation for Solid Rocket Motors

Yanjie Ma, Futing Bao, Weihua Hui, Yang Liu, and Yijie Gao

Science and Technology on Combustion, Internal Flow and Thermo-Structure Laboratory, Northwestern Polytechnical University, Xi'an, Shaanxi 710072, China

Correspondence should be addressed to Weihua Hui; zhongyuancao@163.com

Received 10 August 2019; Revised 4 December 2019; Accepted 14 December 2019; Published 31 December 2019

Academic Editor: Linda L. Vahala

This paper describes a zero-dimensional model for evaluating the mass flow rate history of a solid rocket motor igniter. Based on the results of an igniter-firing experiment, in which the igniter is the only source of combustion gas and no propellant is ignited, the proposed model can be used to compute the mass flow rate of the igniter. Different species and temperature-dependent properties, such as the specific heat for each species, are considered. The coupling between the flow field variables in the combustion chamber and the heat transfer at the gas-solid interface is computed in a segment way. Calculations are performed for different species and properties, and the errors are discussed. Using the computed igniter mass flow rate as a boundary condition, a two-dimensional calculation is performed for validation purposes. The results are in good agreement with experimental data. The proposed model can be used to provide reasonable boundary conditions for solid rocket motor simulations and to evaluate the performance of igniters. Although derived on the basis of a small-scale solid rocket motor, the model has the potential to be used in large-scale systems.

1. Introduction

Although the ignition process occurs for a very short time duration, it plays an important role in the operation of solid rocket motors (SRMs). Extensive studies have investigated the ignition process of SRMs, and numerous models have been proposed. Different subjects, such as the ignition criterion [1–3], flame propagation [4], and fluid-structural coupling during the ignition [5, 6], have been studied by many researchers. As the initial energy source, the igniter gas has a crucial effect on the ignition process. In all the ignition models for SRMs, the mass flow rate (MFR) of the igniter gas is a relevant boundary condition that directly affects the solution of the associated partial differential equations [7]. Hu et al. [8] carried out a series of numerical calculations using the commercial software package ANSYS Fluent and discussed the influence of the igniter MFR on the ignition of an SRM. Results show that changes in the igniter MFR history induce substantial internal ballistic changes in the SRM during the ignition. Thus, for an SRM, it is very important to evaluate the igniter gas MFR history precisely, as this would not only enable better simulations but also allow the performance of the igniter to be assessed for safety or reliability reasons. These are the two primary motivations for this study.

To obtain the igniter MFR history, some researchers have recorded the experimental pressure history of the igniter motor. For large SRMs that use igniter motors, such as space shuttle boost SRMs [9], this approach is feasible. However, for smaller SRMs, including some igniter motors, the pressure data for the igniter are difficult to obtain. Some of these SRMs may use confined igniters, in which the case holding the igniter charge ruptures or melts during ignition. Other SRMs may use unconfined igniters, such as conductive-film igniters, which do not have any case to hold the igniter charge. In these cases, there would be no "igniter motor pressure" to collect in computing the MFR of the igniter gas. Moreover, for these SRMs, different forms of igniter charge, such as powders, granules, pellets, or stripes, may be used instead of grains with regular geometrical configurations. This makes it difficult to predict the igniter MFR by estimating the generation rate of combustion gas, as neither the burning rate nor the burning area is easy to determine. For

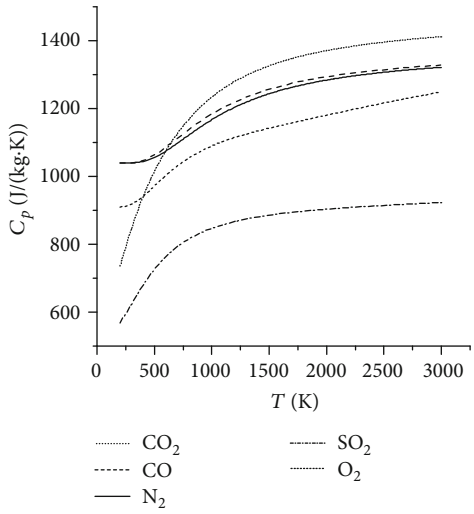

Figure 1: Specific heat as a function of temperature.

these reasons, some studies [10, 11] have used coarse data for the igniter MRF, despite this being a very important boundary condition for ignition simulations. One reason why acceptable results can still be obtained with an inaccurate igniter MFR as the boundary condition is that the ignition process occurs over a very small part of the whole operating duration of an SRM. Even during the ignition, once the main propellant is ignited and the flame begins to propagate, the influences of the igniter gas and initial air on the internal ballistics decrease significantly. Thus, when pressure data from computational results are compared to experimental results, the differences between them during the ignition stage may not be noticed [11–15].

This paper describes a model for evaluating the igniter MFR history using pressure data obtained from an SRM igniter-firing experiment in which only the igniter is fired. For a typical SRM, the initial air, igniter gas, and combustion gas from the main propellant may exist simultaneously in the combustion chamber during the ignition process. In many studies, researchers assume that all three species have the same properties as the propellant combustion gas [8, 9]. However, at the early stage of the ignition process, the fractions of different species change quickly, leading to large variations in the thermophysical properties of the mixture gas. Thus, such a one-species assumption is unrealistic. Other studies have considered the differences between different species in the combustion chamber, although they use constant thermophysical properties for each species. In fact, many gas properties are temperature-dependent. For instance, Figure 1 shows the temperature dependence of the specific heat at constant pressure (C_p) for different species in the temperature range 200–3000 K. As the temperature rises, C_p increases for each species. Specifically, for carbon dioxide (CO_2), the increment can be greater than 90%, from 735.28 J/(kg·K) at 200 K to 1412.25 J/(kg·K) at 3000 K. As a substantial change in C_p would influence the gas energy directly, it is important to consider the C_p-T relationship. In this paper, different gaseous species involved in the igniter-firing experiment are considered according to their chemical formula. For each of these species, the influences of the chamber temperature on the physical properties, such as the specific heat and viscosity, are considered. Another factor affecting the ignition process is the heat transfer between the gas phase and the solid phase. In this study, heat transfer caused by convection and radiation is computed by a simple relation, following numerical calculations of the temperature distribution in the solid phase using a one-dimensional finite volume method (FVM).

2. Theory

The SRM studied in this paper is depicted in Figure 2. The igniter is installed at the head end of the combustion chamber. The original cylindrical grain of double-based propellant is replaced by an "aluminium alloy grain" with the same geometric configuration. The combustion chamber case and the nozzle, as well as the throat lining, are made of steel. A nozzle slug is placed near the exit of the nozzle. In the model for evaluating the igniter MFR history for the SRM, we consider the "combustion chamber" to be the volume from the head end of the chamber downstream to the throat. In this paper, the following primary assumptions are used. (a) The chamber is zero-dimensional. This assumption has been used in many mature models for studying the ignition of SRMs [16, 17] and produces reasonable results as long as the length-to-diameter (L/D) ratio is not too large. (b) The throat is choked immediately after the plug rupture. This assumption simplifies the computation of the MFR out of the chamber shortly after the rupture of the nozzle plug and at the end of the experiment when the chamber pressure is too low to maintain the throat in the choked state. (c) The condensed particles generated from the combustion of the igniter charge are neglected and only the gaseous species are considered. This assumption does not affect the pressure because the condensed particles make no contribution to the chamber pressure. The radiative heat transfer due to the condensed particles is considered by a simplified expression, together with radiation from gaseous species [5]. Based on this assumption, the MFR history the model obtains is actually the gas phase MFR history only. From the results which will be revealed later, this assumption is considered feasible. (d) The igniter gas is assumed to be a frozen flow. The secondary reaction between the flammable species in the igniter gas and the oxygen in the initial air in the combustion chamber is also neglected. However, it is worth noting that the mass fraction of a specific species in the mixture will change as the ratio between the igniter gas and air changes. (e) The volume of the chamber remains unchanged. (f) All species of gas are considered to be ideal gases.

Besides these assumptions, this paper considers several factors that are often neglected. In small SRMs, such as that studied in this paper, the igniter gas MFR plays a more important role than in large SRMs because it constitutes a relatively larger fraction of the whole combustion product. Thus, to obtain more reliable igniter gas MFR data, it is important to consider (a) the initial air in the combustion chamber before the ignition, (b) different species in the

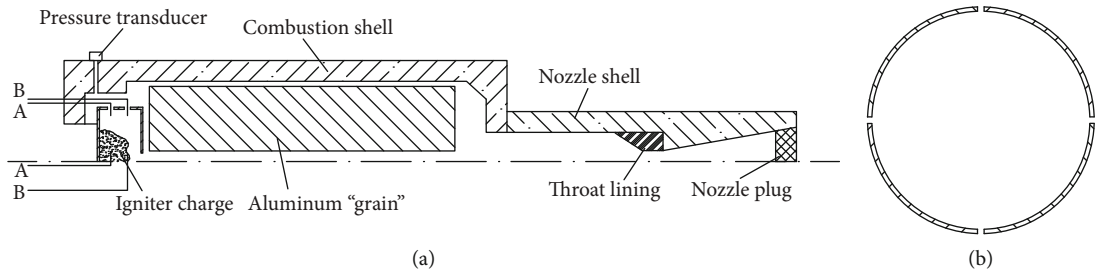

Figure 2: Schematic of the SRM. (a) Longitudinal section of the motor. (b) Igniter cross sections A-A and B-B.

igniter gas, and (c) temperature-dependent physical properties for each species.

2.1. Mass Equation. At any time, the gas flow rate entering the chamber is equal to the MFR of the igniter gas and can be expressed as the derivative of the overall igniter gas with respect to time (dm_{ig}/dt). The MFR out of the chamber, according to assumption (b), can be written as

$$q_m = \begin{cases} 0, & \text{before the slug rupture,} \\ PA_t/c^*, & \text{after the slug rupture.} \end{cases} \quad (1)$$

In this paper, the throat area A_t is assumed to be a constant because the operation time of the SRM is fairly short. The characteristic velocity c^* can be obtained from the expression

$$c^* = \frac{\sqrt{RT}}{\Gamma}, \quad (2)$$

where $\Gamma = \sqrt{k(2/k+1)^{k+1/k-1}}$. Thus, the mass equation for the total mass in the chamber can be written as

$$\frac{dm}{dt} = \frac{dm_{ig}}{dt} - q_m. \quad (3)$$

For the ith species, the MFR entering and exiting the chamber can be written as $x_i(dm_{ig}/dt)$ and $q_m(m_i/m)$, respectively. Hence, the mass equation for the ith species is

$$\frac{dm_i}{dt} = x_i \frac{dm_{ig}}{dt} - q_m \frac{m_i}{m}. \quad (4)$$

2.2. Energy Equation. Neglecting the kinetic and potential energy, the gas energy in the combustion chamber is mC_vT. The rate of change of energy in the combustion chamber can be written as

$$\frac{d}{dt}(mC_vT) = C_{p,f}(T_f)\frac{dm_{ig}}{dt} - q_m C_p(T)T - \sum q_h. \quad (5)$$

The first term on the right-hand side of equation (5) represents the energy increment from the entrance of the igniter gas, where $C_{p,f}(T_f) = \sum_{i=1}^{N} x_i C_{p,i}(T_f)$ is the specific heat of the igniter gas at temperature T_f. The second term on the right denotes the energy loss rate from the outflow. $C_p(T)$ denotes the specific heat of the mixture gas at temperature T. The third term is the heat transfer rate at the gas-solid interface. This is expressed as the sum of the heat transfer at different parts of the interface. The left-hand side of equation (5) can be written as

$$\frac{d}{dt}(mC_vT) = T\sum_{i=1}^{N}\left(C_{v,i}(T)\frac{dm_i}{dt}\right) + B\frac{dT}{dt}, \quad (6)$$

where B is defined as $B = T\sum_{i=1}^{N} m_i(dC_{v,i}/dT) + mC_v(T)$ for simplicity. Substituting equation (6) into equation (5) and combining the mass equations, the energy equation can be rewritten as

$$\frac{dT}{dt} = \frac{1}{B}\left[\left(C_{p,f}(T_f)T_f - C_{v,f}(T)T\right)\frac{dm_{ig}}{dt} - q_m RT - \sum q_h\right], \quad (7)$$

where B has the same meaning as that in equation (6). To compute the heat transfer at the gas-solid interface, the interface is divided into the gas-grain interface, gas-case interface, and gas-nozzle interface according to the flow condition and material used for each solid component. The interface between the combustion gas and the igniter case is neglected for the small scale of the igniter case. For each part of the gas-solid interface, the local heat transfer rate is

$$q_h = hA(T - T_w), \quad (8)$$

where the overall heat transfer coefficient h can be expressed as the sum of the convective transfer coefficient and the radiative transfer coefficient, $h = h_c + h_r$.

For each interface, the convective heat transfer coefficient is computed by the expression

$$h_c = 0.023\mathrm{Pr}^{-2/3}C_p(\mu/D)^{0.2}(\rho u)^{0.8}, \quad (9)$$

where the Prandtl number is given by $\mathrm{Pr} = 4k/(9k-5)$ and the viscosity comes from $\mu = 1.187\times10^{-7}(1000M)^{0.5}T^{0.6}$, where $1000M$ denotes the molecular weight of the mixture gas in the chamber [18]. Although the zero-dimensional assumption is used, it is necessary to evaluate the gas velocity to compute the convective heat transfer coefficient by equation (9). After comparisons with experimental and

two-dimensional numerical results, two different procedures are suggested for evaluating the gas velocity. In the first procedure, the Mach number at some port section is computed from the relation between Ma and the ratio of throat area to section area, assuming that the overall MFR in the port is the same as that through the throat:

$$\frac{A_t}{A_P} = \mathrm{Ma}\left[\frac{2}{k+1}\left(1 + \frac{k-1}{2}\mathrm{Ma}^2\right)\right]^{-1/\mathrm{k}-1}. \quad (10)$$

Solving equation (10) using Newton's iteration method or similar, the gas velocity can be computed from the definition $\mathrm{Ma} = u/\sqrt{kRT_{\mathrm{static}}}$. The static temperature is given by

$$T_{\mathrm{static}} = T\left(1 + \frac{k-1}{2}\mathrm{Ma}^2\right)^{-1}. \quad (11)$$

The second procedure is based on the fact that the volume between the head end of the chamber and the grain is small compared with the downstream volume. Under this assumption, the head end volume requires no gas to increase its pressure and all the igniter gas entering the combustion chamber goes downstream to the aft end volume of the chamber through the ports. This leads to

$$\frac{dm_{\mathrm{ig}}}{dt} = \rho u A_p = \frac{P_{\mathrm{static}}}{RT_{\mathrm{static}}} u A_p, \quad (12)$$

where the static pressure obeys the expression

$$\frac{P_{\mathrm{static}}}{P} = \left(1 + \frac{k-1}{2}\mathrm{Ma}^2\right)^{-k/k-1}. \quad (13)$$

Combining equations (11)–(13), the gas velocity in the ports can be computed. In the ignition process of a real SRM, some gas must be consumed to increase the pressure at the head end, so the MFR in the ports would tend to be overestimated, causing an overestimation of the gas velocity in the ports. However, in real cases, the rate of diffusion is finite and the temperature at the head end of the chamber would be higher than the average temperature of the chamber. Thus, by using the zero-dimensional assumption, the head end temperature will be underestimated. This will overestimate the gas density near the head end of the chamber and negate the velocity overestimation caused by the assumption of zero mass consumption at the head end region. According to the validation calculations, the negation is so strong that the gas velocity is actually underestimated. This causes the convective heat transfer to be slightly underestimated, leading to a smaller igniter MFR.

During the implementation of the model, the larger of the gas velocities computed from the two procedures is used to obtain h_c for the grain and the chamber case. For the long-tail nozzle, the value from the first procedure is used, as the assumption that all gas goes through the nozzle section is not feasible when the volume before the nozzle is too large to be neglected.

The radiative heat transfer coefficient is computed as

$$h_r = C\sigma\left(T^2 + T_w^2\right)(T + T_w), \quad (14)$$

where C is set to 0.25. This value has been used by multiple researchers [6, 9] for radiative heat transfer calculations in the port region.

As shown by equations (8) and (14), to determine the heat transfer at the gas-solid interface, the interface temperature at the solid side (T_w) is also needed. The heat conduction normal to the surface of the solid is solved numerically using a one-dimensional FVM to obtain the temperature at the solid surface. This will be introduced in the next subsection.

2.3. Heat Conduction Solution in Solid Phase. Let y be the coordinate normal to the solid surface, with its positive direction pointing into the solid. The one-dimensional heat conduction in the solid with no heat source can be written as

$$\frac{\partial T_s}{\partial t} = \alpha \frac{\partial^2 T_s}{\partial y^2}, \quad (15)$$

where the thermal diffusivity is expressed as $\alpha = \lambda/\rho_s C_{p,s}$. Because of the large thickness of the chamber case and the nozzle and the short duration of the SRM operation, the temperature at the outer surfaces of the chamber case and the nozzle remains as ambient temperature during the experiment. Thus, Dirichlet boundary conditions are applied at these outer surfaces:

$$T_s(t, L) = T_a. \quad (16)$$

The aluminium alloy grain, as a substitute for the original grain, has a large thermal conductivity, large thermal diffusivity, and small thickness. As both the inner side and outer side of the cylinder are exposed to the combustion gas, half of the thickness normal to the cylinder surface is modelled. By doing so, the boundary away from the combustion gas is considered to be a symmetric boundary, and a Neumann boundary condition is implemented:

$$\left.\frac{\partial T_s}{\partial \mathrm{y}}\right|_L = 0. \quad (17)$$

For each solid boundary adjacent to the combustion gas, a Robin boundary condition is implemented:

$$-\lambda_s \left.\frac{\partial T_s}{\partial \mathrm{y}}\right|_w = h(T - T_w). \quad (18)$$

Once the heat conduction solution has been obtained in the cells of the numerical one-dimensional grid, the temperature at each solid surface is computed from the temperature values of the first two cells by the following expression [19]:

$$T_w = \frac{hT + (\lambda_s/3\Delta y)(9T_0 - T_1)}{h + (8\lambda_s/3\Delta y)}. \quad (19)$$

2.4. Equation of State. Under the assumption of an ideal gas, the gas in the chamber obeys $PV = nR^*T$. Differentiating this expression with respect to time, we have

$$\frac{V}{R^*}\frac{dP}{dt} = T\frac{dn}{dt} + n\frac{dT}{dt}, \tag{20}$$

where dP/dt can be computed by numerical differentiation of the experimental data. Combining the expression for the amount of substance in the chamber $n = \sum_{i=1}^{N} m_i/M_i$ and the mass equation for the ith species (equation (4)), the derivative of n with respect to time can be written as

$$\frac{dn}{dt} = \sum_{i=1}^{N}\frac{1}{M_i}\left(x_i\frac{dm_{\text{ig}}}{dt} - q_m\frac{m_i}{m}\right). \tag{21}$$

Substituting equations (7) and (21) into equation (20), the MFR of the igniter gas can be expressed as

$$\frac{dm_{\text{ig}}}{dt} = \frac{(VdP/R^*dt) + q_mT(nR/B + 1/M) + (n/B)\sum q_h}{(T/M_f + n/B)\left[C_{p,f}(T_f)T_f - C_{v,f}(T)T\right]}, \tag{22}$$

where B has the same definition as in equation (7).

3. Numerical Procedure

The energy expression in equation (8) shows that the flow field variables are coupled with the temperature at the solid surface. A segregated solution approach is implemented to simplify the code. In the segregated solution approach, at each time step, the variables of the flow field in the combustion chamber are computed by solving the equation set composed of equations (7) and (22) using a fourth-order Runge–Kutta method. A one-dimensional FVM is then implemented to update the solid surface temperature using the heat coefficients computed from the flow field variables. The diffusion term in the conduction equation is treated with a central-difference scheme, and the transient term is treated with a first-order implicit scheme. The flow field variables and solid phase temperature distribution are computed alternately until the solution converges, i.e., when the relative error between two successive values of the chamber temperature is less than 10^{-9}. The next time step is then computed.

4. Experiment

The schematic of the SRM for the experiment described in this paper is shown in Figure 2. The original SRM has a free-standing cylindrical grain in which the head and aft ends are insulated and only the inner and outer surfaces burn. To study the igniter in isolation, a grain made of aluminium alloy is used as a substitute. The aluminium alloy grain has the same geometric configuration as the original grain, with a length of 73.5 mm, inner radius of 2.5 mm, and outer radius of 18 mm. The chamber case is made of steel. The inner radius and outer radius of the chamber are 19.25 mm and 35 mm, respectively. The SRM has a long-tail nozzle made of steel with a steel throat lining. The nozzle has a minimum thickness of 6.65 mm. The length of the cylinder segment of the nozzle before the convergent segment is 31 mm and the inner radius is 7 mm. The throat radius is 2.55 mm. The igniter is installed at the head end of the combustion chamber and has an aluminium case. There are nine orifices through which the igniter gas can exit. One orifice faces the axis of the combustion, while the other eight are distributed on the side surface of the cylindrical igniter case. Black powder (75% KNO_3, 15% S, and 10% C) is used as the igniter charge. The mass of the igniter charge is 1.35 g. The experiment is carried out in an ambient temperature of approximately 290 K and an ambient pressure of approximately 0.101 MPa. The pressure transducer mounted midway along the chamber case collects pressure data every 0.5 ms during the experiment. The pressure history obtained in this way is shown in Figure 3.

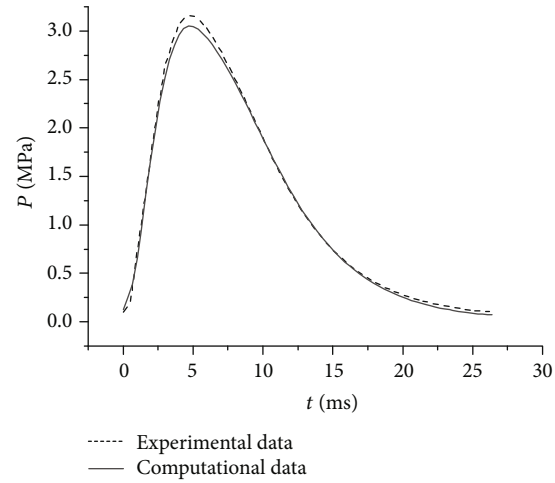

Figure 3: Pressure data from experiment and numerical computation.

5. Results and Discussion

The pressure history obtained from the experiment shows a process consisting of pressurization and depressurization. Initially, the chamber pressure rises quickly, reaching a peak value of 3.16 MPa after about 5 ms. The pressure then decreases to the ambient pressure after about 26.5 ms. Before implementing the numerical computation procedure, the time derivative of pressure (dP/dt) was computed using numerical differentiation, as shown in Figure 4. This not only provides the input data for the computation (see equation (22)) but also determines the corresponding pressure of the nozzle slug rupture and which expression should be used in equation (1) to compute the outflow mass rate. In Figure 4, there is a slight decrease in the rate of change of pressure at about 1 ms. This signifies the rupture of the nozzle plug. Thus, the pressure required to rupture the slug (0.8 MPa) is obtained by reading the pressure value from Figure 3 at 1 ms. After this slight decrease in dP/dt, there is a brief increment as the igniter MFR grows, increasing the net MFR at the

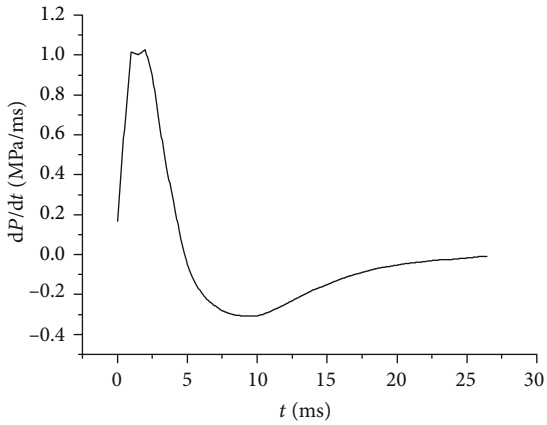

Figure 4: Derivative of pressure versus time.

Table 1: Gas species and their fractions.

Species in igniter gas	Mass fraction
CO_2	0.562687
CO	0.219515
N_2	0.189779
SO_2	0.028019
O_2	0

corresponding time. After that, dP/dt decreases quickly and then climbs slowly to about zero.

In addition to the history of P and dP/dt, the fraction and properties of each species are needed for the computation. The open-source computer program Chemical Equilibrium with Applications (CEA) [20] was used to compute these variables. A rocket problem was solved in CEA, with the pressure set to 3 MPa and the initial temperature of reactants (compositions of black powder) set to 290 K. The results from CEA show that the mass fraction of condensed matter in the products is 43.7%. According to assumption (c), this condensed matter can be neglected, which makes the overall mass of the igniter gas 0.76 g. In the gaseous phase, four pure species, CO_2, CO, N_2, and SO_2, make up 97.2% of the mass; thus, other species are neglected for simplicity. For unity of code writing, O_2 is also considered as a species of the igniter gas, although it has a fraction of zero. The species in the igniter gas are listed in Table 1. The air exists in the chamber as a mixture of O_2 and N_2, with mass fractions of 23.3% and 76.9%, respectively.

The ratio of specific heat at constant pressure to gas constant for each species can be fitted as a function of temperature:

$$\frac{C_p}{R} = a_1 T^{-2} + a_2 T^{-1} + a_3 + a_4 T + a_5 T^2 + a_6 T^3 + a_7 T^4. \quad (23)$$

The coefficients for each species can be obtained from the property database of CEA [20]. After some simple calculations, the value of C_p for each species was obtained, as shown in Figure 1.

Table 2: Properties of solid materials.

Material	Density (kg/m^3)	Specific heat (J/(kg·K))	Heat conductivity (W/(m·K))
Steel	8030	502	16.3
Aluminium alloy	2700	871	205

Two different solid materials, steel and aluminium alloy, were considered in this study. Their properties are listed in Table 2.

After several trials, the time step and cell number were chosen to meet the grid-irrelevant requirement. The time step was set to 0.05 ms. For one-dimensional conduction computations in the solid phase, a cell number of 40 was used for the grain, chamber case, and nozzle.

Before any results are shown, it is worthy to notice that based on assumption (c), we neglect the condensed matter and assume that only the gas phase matter is responsible for the combustion pressure and heat transfer, so the MFR history we obtained by the proposed model is actually only the MFR history of the gas phase matter.

5.1. Results under Different Assumptions. To study the influence of different factors on the results, the code was modified slightly to implement four different computations under different assumptions. Some of these assumptions have been used in different studies. The four cases were as follows. (1) All the gas in the computation has the same properties as the igniter gas (one-species assumption). The effective C_p of the igniter gas is computed at combustion temperature from the CEA calculation results and is assumed to be constant (constant C_p assumption). (2) The gas is considered as the mixture of the igniter gas and air. The specific heats for these two species are computed at combustion temperature and ambient temperature, respectively, and treated as constants. (3) Five chemical species (CO_2, CO, N_2, SO_2, and O_2) are considered. The specific heat for each species is a function of temperature, as expressed in equation (23). In these three cases, the radiative heat transfer is ignored. (4) Same as case (3), except that radiative heat transfer is considered.

The igniter MFR results for all cases are depicted in Figure 5. To aid the discussion, the results are divided and plotted at four different intervals, as shown in Figure 6. The temperature results are shown in Figure 7. Prior to the discussion, it is worth noting that, for the SRM studied in this paper, the igniter gas has a larger molar mass (M) than air and C_p of the igniter gas at the combustion temperature is greater than that of air at ambient temperature. Thus, the one-species assumption in case (1) would lead to an overestimation of M when the air fraction is high, and the degree of the overestimation will decrease as the air fraction decreases because of the entry of igniter gas and exit of air. The constant C_p assumption in case (1) would always cause an overestimation of C_p. In case (2), the influence of the constant C_p

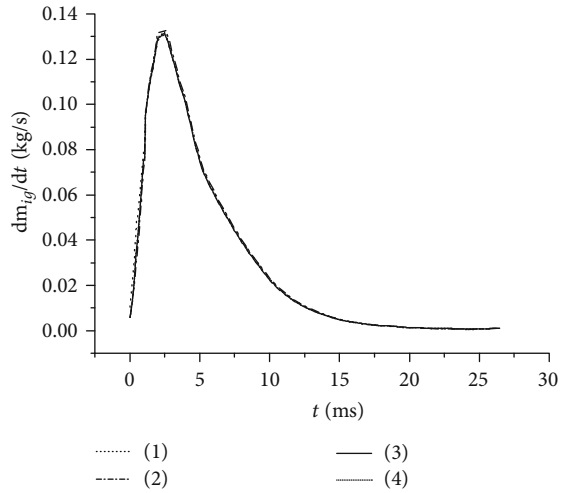

Figure 5: The igniter MFR results computed in different cases.

assumption is a little more complicated. This assumption underestimates C_p in the mixture gas in the chamber when the mass fraction of air is relatively high or the temperature is high (this is true in the first few milliseconds) and then overestimates C_p when the air fraction and temperature drop.

As Figure 5 shows, the MFR results in the four different cases are similar, but when we focus on different time intervals, as shown in Figure 6, there are some details that should be discussed. Before the rupture of the nozzle slug, the greatest igniter MFR occurs in case (1). This is because the overestimated C_p makes it difficult for the temperature to rise (see the temperature history plots in Figure 7). Thus, as determined by the ideal gas law, more substance is needed to maintain the pressure. Moreover, the molar mass is also overestimated in case (1) because of the one-species assumption, which increases the MFR. The situation in case (2) over the same time interval is considerably different. The molar mass difference between the igniter gas and the air is considered in case (2), so the constant C_p assumption is the main cause of inaccuracy in the results. During this time interval, C_p is underestimated for the mixture in the chamber because the air holds a low C_p value that does not increase as the temperature rises. Thus, it is slightly easier for the temperature to rise in case (2) than in the experiment. Consequently, the amount of substance, as well as the MFR of the igniter gas, is underestimated in case (2). This is why the igniter MFR in case (2) remains low at the beginning of the ignition. There are sudden increments in all the plots when the nozzle slug ruptures. This is due to the assumption that the throat is choked immediately after the rupture, causing the outflow rate to increase too soon.

Once the slug fails, the igniter MFR in case (2) climbs to the largest peak of all four cases and continues to produce the highest value until the last few milliseconds. This can be explained by the constant C_p assumption. A short time after the slug fails, the underestimation of C_p leads to a larger ratio of specific heats (k) and consequently a smaller characteristic velocity, which, according to equation (1), causes an overestimation of the outflow rate. Therefore, the igniter MFR must increase to maintain the pressure until both the air fraction and temperature drop sufficiently in the last few milliseconds. In case (1), C_p is overestimated at all points. This leads to a greater value of the characteristic velocity and a smaller outflow rate. Thus, the overestimation of C_p has a negative influence on the igniter MFR in some way. In contrast, as discussed earlier, the overestimation of C_p and the molar mass have positive influences on the igniter MFR, as they do before the rupture of the slug. From the results, we can see that the negative influence is strong over a short time interval after the slug rupture, so the igniter MFR in case (1) has the lowest value, as shown by Figure 6(b). After that, the positive influence seems to become stronger for a few milliseconds, until about 16.5 ms.

In the last few milliseconds of the operation of the SRM, there is little air left in the chamber. The results in cases (1) and (2) become very close. As the temperature drops, C_p in the chamber is increasingly overestimated, leading to an underestimation of the outflow rate. Consequently, the igniter MFR is underestimated in both case (1) and case (2). As shown in Figure 7, in the very last millisecond, the temperature rises again in all cases. This might be caused by assumption (b). Under this assumption, the outflow rate is overestimated by equation (1) while the chamber pressure is actually too low to keep the throat choked. This overestimation would then lead to an overestimation of the igniter MFR (see Figure 6(d)). Thus, more igniter gas enters the chamber, causing the temperature to rise.

In case (3), both the species- and temperature-dependent C_p are considered. Thus, the results should be more accurate than those for cases (1) and (2). The results may be further improved by considering the radiative heat transfer, as we do in case (4). As we can see from Figures 5 and 6, the results in case (4) show that the radiative heat transfer leads to a slightly higher igniter MFR.

As shown in the temperature history results (Figure 7), when the specific heat is considered as a constant, the chamber temperature is dramatically affected. Initially, as C_p is evaluated in opposite ways in cases (1) and (2) (overestimated in case (1) and underestimated in case (2)), the temperature results from (1) and (2) are different from one another. After about 10 ms, once the air fraction has dropped to a low level, the temperature results from cases (1) and (2) become very similar and have moved away from the results obtained in the other two cases.

The overall mass of the igniter gas in the different cases is compared with the experimental value in Table 3. As mentioned earlier, gas phase mass in experiment is 0.76 g. From Table 3, we can see that all the values of total gas mass computed in different cases are close to the experimental value. This is a proof of the reliability of the model.

Yet, the computed values are a little larger than the experimental value. The primary reason for this is that secondary combustion has been neglected. Without considering secondary combustion between the igniter gas and the air, a heat source has been neglected, and so, a larger igniter gas MFR is needed to achieve the pressure history. When the

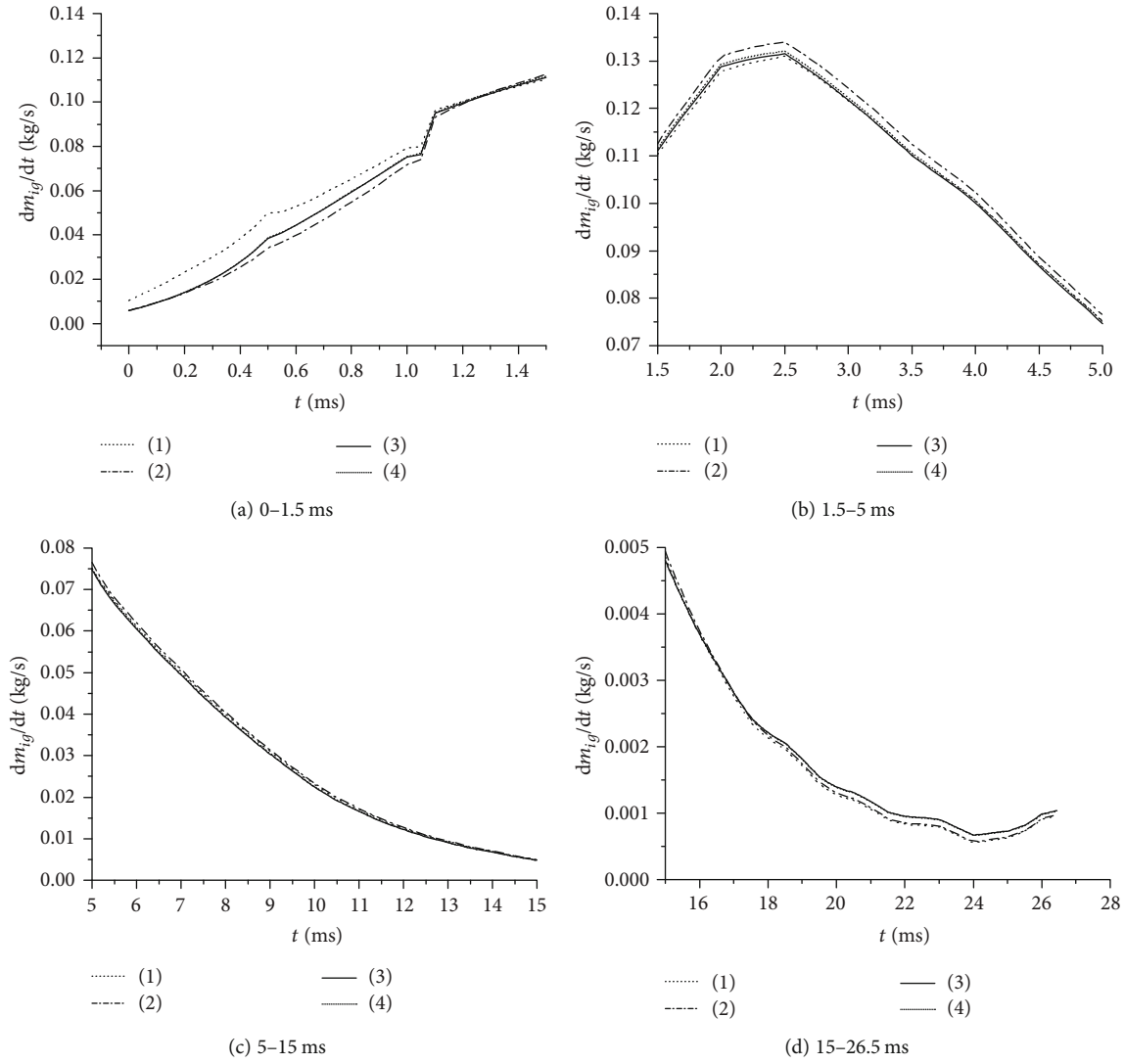

Figure 6: Details of the MFR history in different cases: (a) 0–1.5 ms, (b) 1.5–5 ms, (c) 5–15 ms, and (d) 15–26.5 ms.

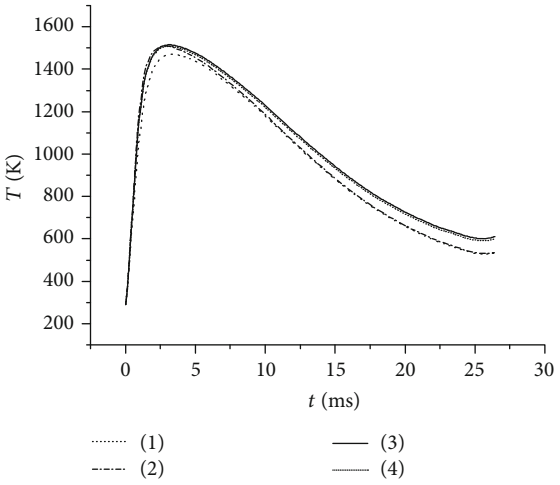

Figure 7: Chamber temperature results computed in different cases.

temperature dependence of C_p is considered, as in cases (3) and (4), the error decreases. Comparing the results in cases (1) and (2), it is apparent that case (1), which includes fewer factors, produces better results. This is because the overall influence of the one-species assumption and the constant C_p assumption on the overall mass acts in opposite ways. Similarly, when the radiative heat transfer is ignored in case (3), the results seem to be better than those in case (4). This is because neglecting the radiative heat transfer negates, to some extent, the influence of neglecting the secondary combustion. If the secondary reaction is also considered based on the assumptions in case (4), we would expect better results than those in case (3). In simulating the ignition or whole operation process of SRMs, some numerical models ignore combustion to decrease the computational burden. If the model proposed in this paper was used to provide a reliable inlet boundary condition to these models, the difference between the computed overall mass and the experimentally

Table 3: Overall mass of the igniter gas computed in different cases.

Cases	Overall mass (g)	Error (%)
1	0.7898	3.92
2	0.7907	4.04
3	0.7795	2.57
4	0.7812	2.79
Experiment	0.7600	0

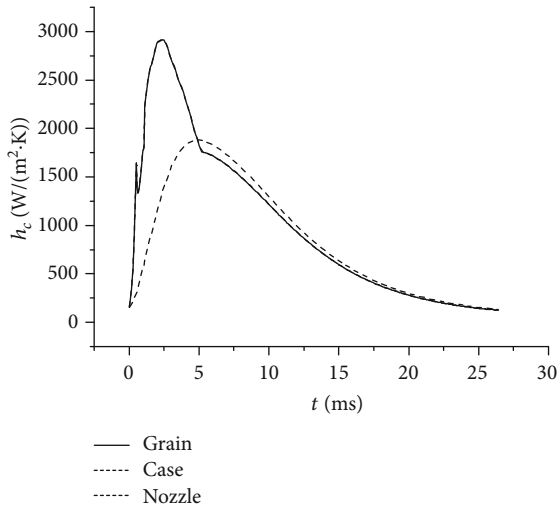

Figure 8: Convective heat transfer coefficient results.

measured mass could be regarded as a reasonable calibration of the igniter MFR.

5.2. Heat Transfer Results. The convective heat transfer coefficient (h_c) results computed in case (4) are shown in Figure 8. The grain and the case have the same value of h_c at all times, as the same variables are used for these two parts. The nozzle has a lower h_c in the first few milliseconds because of the lower gas velocity. After about 5 ms, as the igniter MFR drops, the velocity computed under the assumption that all the igniter mass goes through the ports is lower than that computed from the area ratio procedure. In this case, the velocity in the long-tail nozzle is higher because of the smaller port area, leading to larger values of h_c. Some vibration in the h_c history for the grain and the case occurs at about 1 ms. This is caused by complex changes in the flow field variables because of the nozzle slug rupture. The radiative heat transfer coefficient (h_r) histories are plotted in Figure 9. As we can see, the values of h_r are fairly small compared to h_c.

The temperature histories of the solid-side interfaces of the three different solid components are shown in Figure 10. The different plots indicate similar behavior, rising up quickly over the initial 10 ms when the overall heat transfer is large and then dropping down slowly. As different materials are used for the grain and the case, their interface temperatures differ from each other. The aluminium grain has much better thermal conductivity than the case and

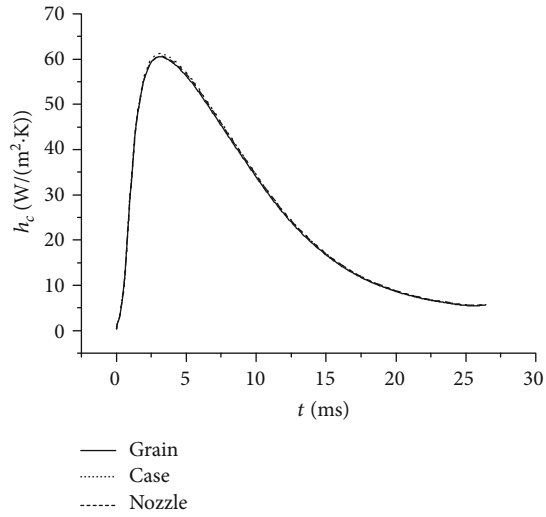

Figure 9: Radiative heat transfer coefficient results.

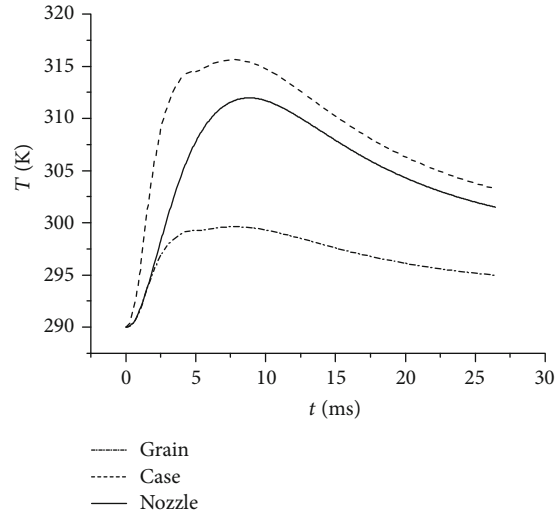

Figure 10: Interface temperature histories.

nozzle, and thus, the conduction in the aluminium grain proceeds more quickly, making the surface temperature lower. The temperature distributions in the solid phase at different times are plotted in Figures 11–13. For clarity, the maximum coordinate values in the case and the nozzle are restricted to the thickness of the grain.

5.3. Validation of the Model. Besides the total mass of gas phase agreement with experiment (Table 3), a two-dimensional axisymmetric numerical calculation was implemented to validate the model proposed. The commercial software package Fluent 6.3 is used for the calculation. During the calculation, the mass flow rate history obtained in case (3) was used as a mass flow inlet boundary condition. The main procedure is similar to that described in Ref. [8]. Both the fluid and the solid were modelled. In the fluid domain, the Favre-averaged Navier–Stokes equations,

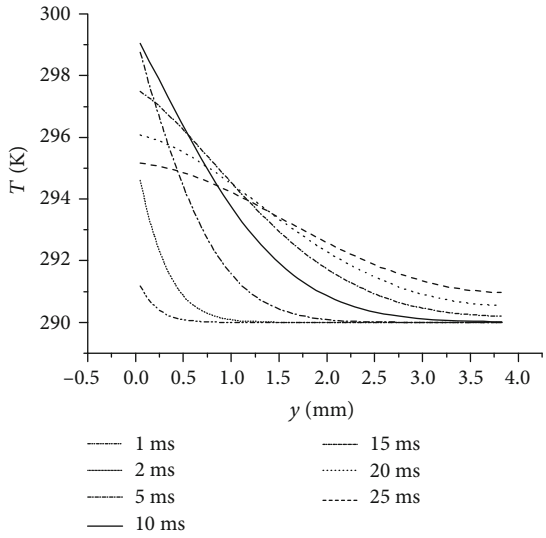

Figure 11: Temperature distribution in the grain.

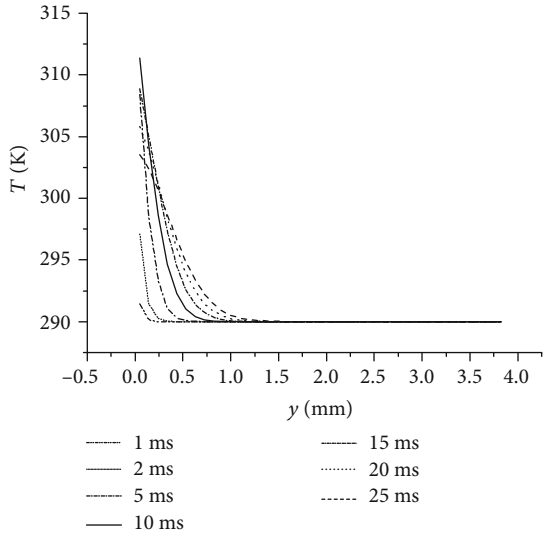

Figure 12: Temperature distribution in the case.

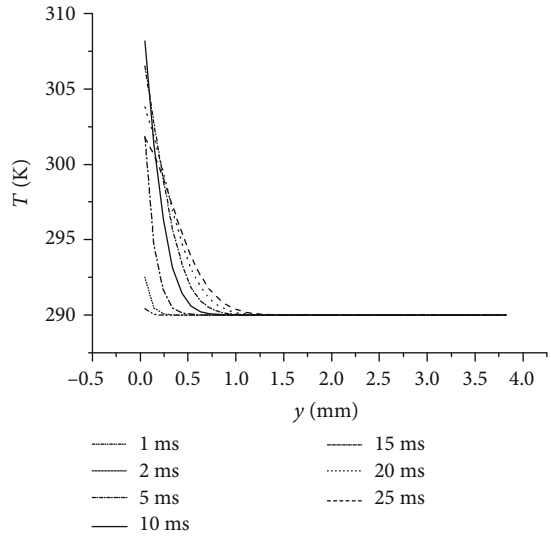

Figure 13: Temperature distribution in the nozzle.

combining the popular turbulent two-equation k-ε model, were solved. In the solid domain, the heat conduction was calculated. One of the main differences from the models used in Ref. [8] is that, in the proposed model, the grain does not combust. Combustion of the grain is beyond the scope of this paper, so no combustion gas from the grain is added to the fluid domain. Another difference is that we are interested in the species and properties, so a species transportation model with no reaction is used and the gas phase has temperature-dependent properties. The outlet of the igniter was set to be a mass flow inlet. The igniter MFR history was fitted by cubic spline interpolation before being applied to Fluent as a user-defined function. After some mesh-independence trials, a grid with 121,195 cells was used. A time step of 1×10^{-6} s was set to ensure that the solution in each time step converged, with the residual for each variable dropping below 10^{-3}.

The pressure results obtained from the two-dimensional calculation are shown in Figure 3. As we can see, the pressure history from the calculation is in good agreement with the experimental data. The peak pressure value is 3.06 MPa, representing a relative error of approximately 3.13% with respect to the experimental data. This implies that the model proposed in this paper is sufficiently reliable to provide a reasonable igniter MFR history.

6. Conclusion

A zero-dimensional model was established to evaluate the igniter mass flow rate from an igniter-firing experiment. The different species in the igniter gas and air initially present in the combustion chamber were considered. For each species, the specific heat was treated as a function of temperature, rather than a constant. The heat transfer due to convection and radiation was also considered. The coupling between the flow field and solid temperature distribution was solved using a segregated solution approach. A comparison of the results computed under different assumptions shows that considering the species and temperature dependence of specific heat reduces the error in the simulations.

The total gas phase mass values from the model and experiment agree well. Combustion chamber pressure history computed by the two-dimensional simulation using the obtained data as boundary condition is close to experiment data. These facts indicate the reliability of the proposed model.

Secondary combustion is not currently considered in the proposed model, but this might have a substantial influence on the process. To improve the model, secondary combustion should be included. For now, the difference between the overall igniter gas mass given by the calculation and experiments can be regarded as calibration data for the pressure change.

The proposed model can be used to provide an accurate boundary condition for numerical computations involving the ignition of SRMs. It also offers an approach for assessing the performance of igniters. Though this model was developed based on the analysis of a small SRM, we believe it could also be used in larger ones.

Nomenclature

A: Area (m^2)
c: Speed of sound (m/s)
c^*: Characteristic velocity (m/s)
C: Empirical constant used for radiative heat transfer coefficient calculation
C_p: Specific heat at constant pressure (J/(kg·K))
C_v: Specific heat at constant volume (J/(kg·K))
D: Characteristic length (m)
h: Overall heat transfer coefficient ($W/(m^2 \cdot K)$)
h_c: Convective heat transfer coefficient ($W/(m^2 \cdot K)$)
h_r: Radiative heat transfer coefficient ($W/(m^2 \cdot K)$)
i: Species index
k: Ratio of specific heats
L: Thickness of solid phase (m)
m: Mass of gas in the combustion chamber (kg)
M: Molar mass (kg/mol)
Ma: Mach number
m_{ig}: Overall mass of igniter gas entering the combustion chamber (kg)
n: Amount of substance (mol)
N: Total number of species considered
P: Chamber pressure (MPa)
Pr: Prandtl number
q_h: Heat transfer rate (W)
q_m: Mass flow rate out of the combustion chamber (kg/s)
R: Gas constant (J/(kg·K))
t: Time (s)
T: Temperature (K)
u: Gas velocity (m/s)
V: Volume of combustion chamber (m^3)
x: Mass fraction of a species in igniter gas
y: Coordinate normal to the solid surface (m)
Δy: Cell size of grid in solid phase
α: Thermal diffusivity (m^2/s)
Γ: Coefficient, a function of k
λ: Thermal conductivity (W/(m·K))
μ: Dynamic viscosity (Pa·s)
ρ: Density (kg/m^3)
σ: Stefan–Boltzmann constant (5.67×10^8 $W/(m^2 \cdot K^4)$).

Subscripts and Superscripts

*: Universal variable
0: Variable for air, index of the solid cell adjacent to gas-solid interface
1: Index of the solid cell one-cell away from the gas-solid interface
a: Ambient
f: Variable for igniter gas
p: Variable in port
s: Solid variable
static: Static variable
t: Variable at throat
w: Variable at the solid surface adjacent to the combustion gas.

Data Availability

Underlying data can be obtained by contacting the corresponding author.

Conflicts of Interest

The authors declare that there is no conflict of interest regarding the publication of this paper.

References

[1] J. H. Frazer and B. L. Hicks, "The thermal theory of ignition of solid propellants," *The Journal of Physical and Colloid Chemistry*, vol. 54, no. 6, pp. 872–876, 1950.

[2] T. L. Jackson and J. Buckmaster, "Heterogeneous propellant combustion," *AIAA Journal*, vol. 40, no. 6, pp. 1122–1130, 2002.

[3] R. Anderson, R. S. Brown, G. T. Thompson, and R. W. Ebeling, "Theory of hypergolic ignition of solid propellants," in *Heterogeneous Combustion Conference*, Palm Beach,FL,U.S.A., December 1963.

[4] G. D. Luke, M. A. Eagar, and H. A. Dwyer, "Ignition transient model for large aspect ratio solid rocket motors," in *32nd Joint Propulsion Conference and Exhibit*, Lake Buena Vista, FL, U.S.A, July 1996.

[5] W. A. Johnston and J. W. Murdoc, "Flow-structural interaction inside a solid rocket motor during ignition transient," *Journal of Propulsion and Power*, vol. 11, no. 5, pp. 998–1005, 1995.

[6] Q. Li, P. Liu, and G. He, "Fluid-solid coupled simulation of the ignition transient of solid rocket motor," *Acta Astronautica*, vol. 110, pp. 180–190, 2015.

[7] A. Peretz, K. K. Kuo, L. H. Caveny, and M. Summerfield, "Starting transient of solid-propellant ocket motors with high internal gas velocities," *AIAA Journal*, vol. 11, no. 12, pp. 1719–1727, 1973.

[8] B. Hu, B. Wang, and X. Tian, "Numerical modeling and studies of ignition transients in end-burning-grain solid rocket motors," *Journal of Propulsion and Power*, vol. 32, no. 6, pp. 1333–1342, 2016.

[9] M. Salita, "Modern SRM ignition transient modeling (part 1): introduction and physical models," in *37th Joint Propulsion Conference and Exhibit*, Salt Lake City, UT, U.S.A., July 2001.

[10] S. T. Chang, S. Han, and J. C. Chai, "Radiation effects on 1-D ignition transient analysis of SRM," in *32nd Joint Propulsion Conference and Exhibit*, Lake Buena Vista, FL, U.S.A., July 1996.

[11] M. D. Giacinto, E. Cavallini, and B. Favini, "Parametric study on solid rocket motor ignition transient and pressure oscillations onset," *Journal of Propulsion and Power*, vol. 31, no. 4, pp. 1117–1126, 2015.

[12] A. M. Tahsini, "Ignition transient simulation in solid propellant rocket motors," in *45th AIAA Aerospace Sciences Meeting and Exhibit*, Reno, Nevada, January 2007.

[13] L. d'Agostino, L. Biagioni, and G. Lamberti, "An ignition transient model for solid propellant rocket motors," in *37th Joint Propulsion Conference and Exhibit*, Salt Lake City, UT, U.S.A., July 2001.

[14] L. H. Caveny, K. K. Kuo, and B. W. Shackelford, "Thrust and ignition transients of the space shuttle solid rocket motor," *Journal of Spacecraft and Rockets*, vol. 17, no. 6, pp. 489–494, 1980.

[15] A. Javed and D. Chakraborty, "Universal erosive burning model performance for solid rocket motor internal ballistics," *Aerospace Science and Technology*, vol. 45, pp. 150–153, 2015.

[16] S. Soto and H. A. Friedman, "Flame spreading and ignition transients in solid grain propellants," *AIAA Journal*, vol. 3, no. 3, pp. 405–412, 1965.

[17] D. M. Adams, "Igniter performance in solid-propellant rocket motors," *Journal of Spacecraft*, vol. 4, no. 8, pp. 1024–1029, 1967.

[18] D. K. Huzel and D. H. Huang, *Design of Thrust Chambers and Other Combustion Devices in: Modern Engineering for Design of Liquid-Propellant Rocket Engines*, Progress in Astronautics and Aeronautics, AIAA, Washington, DC, 1992.

[19] S. Mazumder, *Numerical Methods for Partial Differential Equations*, Academic Press, London, 2017.

[20] S. Gordon and B. McBride, *Computer Program for Calculation of Complex Chemical Equilibrium Compositions and Applications*, NASA Publication 1311, Cleveland, Ohio, 1994, Pts. 1-2.